PCCP

Check for updates

Tunable particle-agglomeration and magnetic coupling in bi-magnetic nanocomposites†

Pierfrancesco Maltoni, [ID] *[a] Miran Baričić, [ID] ‡[b] Gianni Barucca, [ID] [cd] Maria Chiara Spadaro,[c] Jordi Arbiol, [ID] [ef] Nader Yaacoub,[g] Davide Peddis [ID] *[bd] and Roland Mathieu [ID] *[a]

A set of non-stoichiometric Zn–Co-ferrite nanoparticles (NPs) was prepared by thermal decomposition of metallic complexes, in the presence of oleic acid, and, after a ligand-exchange process, was coated by a hydrophilic surfactant: these NPs were used as seeds in a sol–gel self-combustion synthesis to prepare nanocomposites (NCs) with a fixed weight ratio. Our focus here is the development of an efficient synthetic approach to control the magnetic coupling between a hard-magnetic matrix (Sr-ferrite) and NPs. The physico-chemical synthetic conditions (temperature, pH, colloidal stability) were optimized in order to tune their effect on the final particles' agglomeration in the matrix. We demonstrate that our synthetic approach is a novel way to produce strongly magnetically coupled NCs, where the final extrinsic properties could be tuned by controlling (i) the agglomeration of seeds in the matrix and (ii) their elemental doping.

Introduction

Bi-magnetic nanocomposites (NCs) have gained a lot of interest over the last years, due to the possibility to finely control and modify their features at the nanoscale by combining two prototypical phases.[1] The novel properties arise from interfacial physical effects, owing to the coupling interaction between the oxides' interfaces which can be tuned *via* structural and morphological modification. Thus, composites represent a new class of materials, owing to the combination of electronic and magnetic properties, which find applications as multiferroics, catalysts, magnetorheological materials and new permanent

magnets.[2–6] The main challenge is to design advanced synthetic approaches to obtain homogeneously-dispersed systems at the nanoscale. Among the several techniques to synthesize nano-particles (NPs), sol–gel chemistry has emerged as an advantageous way to prepare transition-metal oxides from homogeneous solutions containing the precursors,[7] and found application in a wide range of nanomaterials (*e.g.*, thin-films,[8] monodisperse nanoparticles,[9] nanocomposites[10]). The main advantage of the sol–gel method is to enable the complete conversion of precursors which is normally prevented in solid-state methods, a solid being limited by mass transport.[11] A possible way to tune the sol–gel process, relies upon the choice of molecular species for the starting solution, as the key to controlling the morpho-structural features of the products, and thus designing novel systems. In the search for alternate ways to reduce the size down to the nanoscale, and explore novel properties (stemming from the large surface energy and size effects), the citrate–gel process is a well-established approach to prepare magnetic nanomaterials such as hexagonal- and spinel-like ferrites:[12–14] the low-temperature treatment permits to retain the single-domain size of the resulting sintered agglomerates, essential for technological applications.[15–17] Furthermore, combining two or several magnetic phases was demonstrated to be an efficient way to achieve superior magnetic performances.[5,18,19] Within this framework, the need for sharp interfaces with large contact areas to maximise the magnetic interactions between particles has required the development of more advanced synthetic strategies to control particle agglomeration, and thus morpho-structural features.

[a] *Department of Materials Science and Engineering, Uppsala University, Box 35, Uppsala, 751 03, Sweden. E-mail: pierfrancesco.maltoni@angstrom.uu.se, Roland.Mathieu@angstrom.uu.se*

[b] *Dipartimento di Chimica e Chimica Industriale & INSTM, nM2-Lab, Università degli Studi di, Genova, Via Dodecaneso 31, Genova, 1-16146, Italy. E-mail: Davide.Peddis@unige.it*

[c] *Dipartimento di Scienze e Ingegneria della Materia dell'Ambiente ed Urbanistica – SIMAU, Università Politecnica delle Marche, Ancona 60131, Italy*

[d] *Consiglio Nazionale delle Ricerche, Istituto di Strttura della Materia, nM2-lab, Monterotondo Scalo (RM), 00015, Italy*

[e] *Catalan Institute of Nanoscience and Nanotechnology (ICN2), CSIC and BIST, Campus UAB, Bellaterra, 08193, Barcelona, Catalonia, Spain*

[f] *ICREA, Pg. Lluís Companys 23, 08020, Barcelona, Catalonia, Spain*

[g] *Le Mans Université, Institut des Molécules et Matériaux du Mans, CNRS UMR-6283, Avenue Olivier Messiaen, Le Mans, 72085, France*

† Electronic supplementary information (ESI) available. See DOI: https://doi.org/10.1039/d3cp03689h

‡ Current address: Laboratoire Interfaces Traitements Organisation et Dynamique des Systèmes, Université Paris Cité, CNRS UMR-7886, 75013 Paris, France.

This journal is © the Owner Societies 2023

Phys. Chem. Chem. Phys., 2023, **25**, 27817–27828 | 27817

Recent studies have reported several ways to enhance the magnetic properties of ferrites *via* chemical composition,[20–24] owing to the flexible crystal structure of such ferrites that easily enables the modification of the cationic distribution, and in turn the magnetic anisotropy; specifically, an increase of saturation magnetization for Zn^{2+} substituted spinel ferrites.[25–27] Hence, in this study, we present a novel way to prepare a set of bi-magnetic NCs by the citrate–gel method by including pre-formed seed NPs ($Co_xZn_yFe_{3-(x+y)}O_4$) in a matrix ($SrFe_{12}O_{19}$), after annealing the composite in air. A previously employed sol–gel self-combustion synthesis was modified,[5,28] by tuning the initial colloidal stability of the seeds *via* changing the pH, controlling the final size of the NPs in the resulting powder-like binary composite. A non-toxic natural catechol ligand (*i.e.*, di-hydro caffeic acid, DHCA) which recently gained interest for biomedical functions,[29,30] was chosen to functionalize the surface of seeds obtained by thermal decomposition.[31] The use of this hydrophilic coating enabled us to tune the stability of NPs by controlling the acid dissociation of DHCA through basis addition.[32] We show that controlling the agglomeration of seeds in the matrix by chemical synthesis is an efficient way to tune the magnetic coupling in the resulting composites. In this context, our main purpose is to improve the chemical synthesis and shed light on the strength of magnetic coupling deriving from the partial agglomeration of seeds in the NCs obtained in different pH conditions. An undoped Co–ferrite sample was prepared as a reference, and the change of magnetic anisotropy in the composite is discussed according to the elemental doping of seeds.

Experimental

Synthesis of $Co_xZn_yFe_{3-(x+y)}O_4$ seeds

The synthesis of $Co_xZn_yFe_{3-(x+y)}O_4$ seeds NPs of 6(1) nm was carried out using standard thermal decomposition of metallic complexes in a high-boiling solvent under an inert atmosphere in the presence of stabilizing surfactants (see Section 1.1 of ESI†).[33] The Fe/Co/Zn precursors ratio has been chosen to obtain $Zn_{0.4(1)}Co_{0.5(1)}Fe_{2.1(1)}O_4$ and $Co_{1.0(1)}Fe_{2.0(1)}O_4$ (referred to as CZFO and CFO, respectively). The amount of Zn was chosen since Co–Zn ferrites from thermal decomposition synthesis are expected to increase their saturation with Zn^{2+} up to $Zn_{0.4-0.5}Co_{0.6-0.5}Fe_2O_4$ (see also Fig. S2, ESI†).[25,26] Table 1 reports the samples' details.

Synthesis of $SrFe_{12}O_{19}$ matrix

The strontium ferrite $SrFe_{12}O_{19}$ matrix (SFO) was prepared by a sol–gel combustion process.[12,28] The pH effect upon the final compound was evaluated by preparing SFO at pH = 4, 7 and 10. (see Section 1.2 of ESI†).

Synthesis of bi-magnetic NCs

The sol–gel self-combustion synthesis was slightly modified to include the seed NPs in the SFO matrix as follows (Fig. 1). Firstly, a ligand-exchange process has been performed to replace the hydrophobic coating (oleic acid) with a hydrophilic layer (di-hydro caffeic acid, DHCA) using tetrahydrofuran (THF)
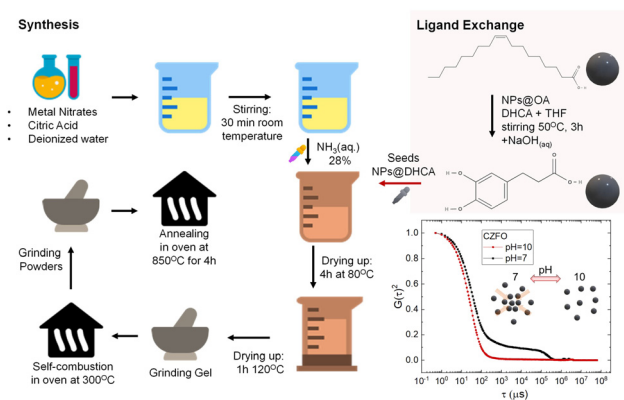

Fig. 1 Synthesis path of nanocomposites (NCs); on the right, the ligand-exchange process is illustrated. The stability of particles' suspension at pH = 10 compared to pH = 7 is shown in the bottom panel, using dynamic light scattering data.

(see procedure described in Section 5 of ESI†).[34] After dissolving the precursors of SFO in a Teflon beaker and adding the citric acid, the seeds NPs (previously stabilized in a basic NaOH aqueous dispersion) are added to the dispersion while adjusting the pH to the final desired value (pH = 7 and 10 were considered in this study). After the mass correction accounting for the coating of the seeds by thermogravimetry (TG), the final estimated weight fraction of seeds added to the synthesis with respect to SFO is around 7 wt%. Next, it is heated in a silicon oil bath to 80 °C for ~ 4 h to form a gel, and then let it quickly dry for 1 h at 120 °C. Next, the dried gel is ground to guarantee the homogeneity of the phases and burnt in a pre-heated oven at 300 °C. The resulting powders are ground and annealed at 850 °C for 4 h under air with a ramp of 5 °C min^{-1}. We refer to the final nanocomposites as NC@CZFO@pH10 (with CZFO seeds, pH = 10), NC@CZFO@pH7 (with CZFO seeds, pH = 7) and NC@CFO@pH10 (with CFO seeds, pH = 10).

Physical, structural, and magnetic characterization

The powder samples were characterized by using a Bruker D8 Advance diffractometer (solid state rapid LynxEye detector, Cu Kα radiation, Bragg–Brentano geometry, DIFFRACT plus software) in the $10°–140°$ 2θ range with a step size of $0.013°$ (counting time was 4 s per step). The powder samples were grounded in an agate mortar and suspended in ethanol. A Si substrate was covered with several drops of the resulting suspension, leaving randomly oriented crystallites after drying. Rietveld analysis was performed on the X-ray powder diffraction (XRPD) data by using the FULLPROF program.[35] The diffraction peaks were described by a modified Thompson–Cox–Hastings pseudo-Voigt function. A peak asymmetry correction was made for angles below $40°$ (2θ). Background intensities were estimated by interpolating a set of points. In the model, seeds were described as cubic $Fd\bar{3}m$ space group. For CFO, the tetrahedral (Td) and octahedral (Oh) sites were assumed to be fully occupied, with $2/3$ Fe^{3+} and $1/3$ Co^{2+}. Since Fe and Co are indistinguishable from XRPD (electron scattering density is the same), we assume a random distribution along tetrahedral

27818 | *Phys. Chem. Chem. Phys.*, 2023, **25**, 27817–27828

This journal is © the Owner Societies 2023

and octahedral sites. For CZFO, the cationic distribution was assumed to be $(Zn_{0.32}Fe_{0.68})_{Td}[Zn_{0.08}Co_{0.46}Fe_{1.46}]_{Oh}O_4$ (according to a recent study by some of the authors[25]). SFO was modelled as a hexagonal $P6_3/mmc$ space-group. The composites were refined accordingly. A NIST LaB$_6$ 660b standard was measured under the same conditions as the samples to account for the instrumental contribution to the peak broadening.

Structural and morphological investigations were performed *via* high-resolution transmission electron microscopy (HRTEM) and scanning transmission electron microscopy (STEM) in high-angle annular dark-field mode (HAADF). These studies were achieved on a field emission gun FEI Tecnai F20 microscope. STEM analysis was combined with electron energy loss spectroscopy (EELS) in the Tecnai microscope by using a GATAN QUANTUM energy filter in order to obtain compositional maps. For electron microscopy measurements, samples, in powder form, were dispersed in ethylic alcohol and submitted to ultrasonic agitation for one minute. Then, a drop of the suspension was deposited on a commercial holey carbon-coated TEM grid and kept in the air until complete alcohol evaporation.

^{57}Fe Mössbauer spectra were recorded using a ^{57}Co/Rh γ-ray source mounted on an electromagnetic transducer with velocity modulated according to a triangular waveform. The spectra were obtained at 300 and 77 K without external applied field. The hyperfine structure was modeled by means of a least-square fitting procedure involving Zeeman sextets composed of Lorentzian lines. The isomer shift (IS) values were referred to that of α-Fe at 300 K.

Dynamic Light Scattering (DLS) measurements were performed with a Malvern Zetasizer Nano ZSP equipped with a 10 mW He–Ne red laser (632.8 nm), operating in backscattered geometry (173°). The suspensions of NPs were analysed in plastic disposable cuvettes after filtration and sonication. More information about the measurements is reported in Section 6 of ESI.†

Elemental analysis was performed by X-ray fluorescence (XRF) on the selected composites, showing only slight deviations from the target composition. Stoichiometric SFO and CFO powder samples were adopted as standards for the analysis, by checking their atomic composition (Fe/Sr = 12 and Fe/Co = 2) by inductively coupled plasma optical emission spectroscopy (ICP-OES). The estimation of spinel ferrite NPs weight fractions was carried out as reported in Section 7 of ESI.† The elemental composition of seeds NPs was confirmed by ICP-OES.

Magnetic measurements were performed at room and low temperature ($T = 300$ and 5 K, respectively) by using a Quantum Design superconducting quantum interference device (SQUID) and Physical Property Measurement System (PPMS) with Vibrating Sample Magnetometer (VSM) option magnetometers, which can supply maximum fields of 5 T and 9 T, respectively. To avoid any displacement of the nano-powders during the measurements, the samples were immobilized in a chemical neutral ethyl cyanoacrylate glue (no significant magnetic contribution from the glue was observed). Isothermal field-dependent magnetization loops were recorded by sweeping the field in the
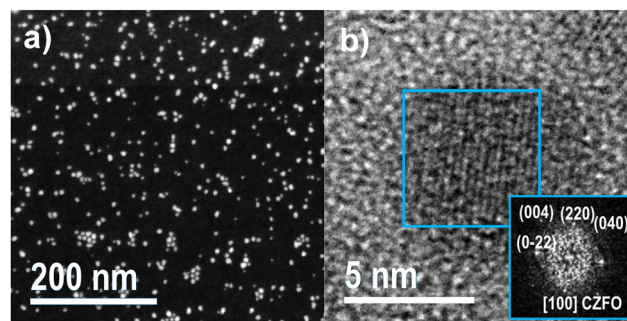

Fig. 2 $Co_{0.46}Zn_{0.40}Fe_{2.14}O_4$ (CZFO) seeds: (a) STEM-HAADF image showing the shape and size of nanoparticles; (b) high-resolution TEM image of a nanoparticle revealing the atomic planes. Inset is the Fast Fourier Transform of the squared area demonstrating the spinel structure of the seeds.

−5T to +5T range, and the obtained magnetization values were normalized by the weight of powders present in the sample and expressed in A m² kg⁻¹. To get information about the irreversible processes, direct current demagnetization (DCD) remanence curves were measured by applying and removing a progressively higher DC reverse field to a sample previously saturated under a (negative) field of −5T and by recording, for each step, the value of the remanent magnetization, M_{DCD}, which is then plotted as a function of the reverse field. The corresponding switching field distributions (SFDs) were obtained from the first order derivative of the M_{DCD} curves. We refer to the average switching field as H_{SW}.

Results and discussion

Tuning particle-agglomeration

The thermal decomposition method has allowed the preparation of monodisperse, highly uniform spherical CZFO NPs. A typical STEM-HAADF image of the CZFO seeds is shown in Fig. 2(a). The NPs have a spherical shape with a uniform diameter of about 5.4 nm ± 1.4 nm, in agreement with XRPD analysis (see Section 3 of ESI† for more details). The seeds are well crystallized as evidenced by HRTEM analysis showing the atomic planes extending on the entire particle size, Fig. 2(b). The inset of Fig. 2(b) is the Fast Fourier Transform (FFT) of the image and allows to identify the cubic spinel structure of the particle. The composition of the seeds was confirmed by STEM-EELS compositional maps, and a uniform distribution of Zn was observed, Fig. S4 (ESI†). From the ZFC/FC curves (see Section 4.1 of ESI†), the extracted maximum temperature, irreversible temperature, and average blocking temperature (T_{max}, T_{irr} and T_b respectively) were found to decrease for CZFO, due to the lowering of anisotropy upon replacement of Co^{2+} with Zn^{2+}, as reported in Table 1. This effect is indeed accompanied by the corresponding decrease of the coercivity H_C.[26,27] Mössbauer spectrometry confirmed the dynamic properties of CZFO, highlighting the presence of sextets in the spectrum at 77 K, which account for the larger fractions of blocked NPs (see Section 4.3 of ESI†), in comparison to the large singlet at 300 K typical of unblocked, *i.e.* superparamagnetic, NPs (or for particles whose relaxation time is near the measurement time scale).

This journal is © the Owner Societies 2023

Phys. Chem. Chem. Phys., 2023, **25**, 27817–27828 | **27819**

Table 1 Composition from ICP-OES analysis, maximum temperature (T_{max}), irreversible temperature (T_{irr}), and average blocking temperature (T_b) from ZFC–FC curves, coercive field ($\mu_0 H_C$), saturation magnetization (M_S^{5T}) and reduced remanent magnetization (M_R/M_S^{5T}) from magnetization (M) vs. temperature (T) at 5 K, and calculated anisotropy constant (K_{eff}). See ESI for magnetic curves

Sample	CFO	CZFO
Composition	$Co_{1.04}Fe_{1.96}O_4$	$Co_{0.46}Zn_{0.40}Fe_{2.14}O_4$
T_{max} (K)	256(7)	197(6)
T_b (K)	178(5)	140(4)
T_{irr} (K)	264(7)	208(6)
$\mu_0 H_C$ (T)	0.90(1)	0.53(1)
M_S^{5T} (A m^2 kg^{-1})	90(1)	100(1)
M_R/M_S^{5T}	0.57(1)	0.60(1)
K_{eff} (J m^{-3})	$7.8(4) \times 10^5$	$4.8(2) \times 10^5$

The CZFO NPs underwent a ligand-exchange process which permitted their controlled partial agglomeration upon tuning the pH conditions of the starting aqueous suspension (given by the presence of citric acid as a chelating agent).[36] This enabled us to exploit the chemical structure of DHCA in a specific range, pH = 7–10, for which citric acid is completely deprotonated.[37] Replacing the hydrophobic coating (oleic acid) with the hydrophilic one (DHCA), did not only allow us to obtain stable suspensions of nanoparticles in water, but provided one more degree of freedom to tune the morphology of the seeds. DHCA has three dissociation constant pK_a (4.5, 9.4 and 11.7),[38] allowing us to tune the degree of deprotonation by simply adjusting the acidic/basic water suspension, which in turn affects the stability of NPs in water.[38] Moving from a neutral (i.e., pH = 7) environment to basic (i.e., pH = 10) environment, yields a larger deprotonation of DHCA, being well above the second acid pK_a (with a corresponding total deprotonation of the carboxylic moiety, and more than 50% of the catechol), and a consequent larger electrostatic stability due to the higher repulsion between the ligand molecules, which are likely attached to the NPs surface through both the carboxylic and the catechol functional groups.[39] While at pH = 7 the lower stability favours a higher degree of agglomeration, with a consequent growth of larger crystallites during the annealing step, compared to those at pH = 10. As a result, the partial agglomeration of CZFO NPs was evidenced by DLS measurements, which highlight a multiple distribution decay of the correlation function for pH = 7 (Fig. 1 and ESI,† Section 6).[40] The subsequent addition to the sol–gel self-combustion route, during the pH adjustment-step, resulted in an effective way to control the initial stability of CZFO particles and thus their final size in the composite after the annealing step, which causes a different growth of this phase in the SFO matrix.

Rietveld analysis of XRPD patterns for NC@CZFO@pH10 and NC@CZFO@pH7, Fig. 3(a) and (b) respectively, reveals that the average crystallite size of the spinel fraction increases to 32(4) nm and to 57(5) nm, respectively (see Table 2); interestingly, the SFO fraction increases as well, although we have observed that the size of SFO (without seeds) seems rather insensitive to the change of pH from 10 to 7 (see Section 3 of ESI†).[42,43] Therefore, it is likely to be the segregation of the two
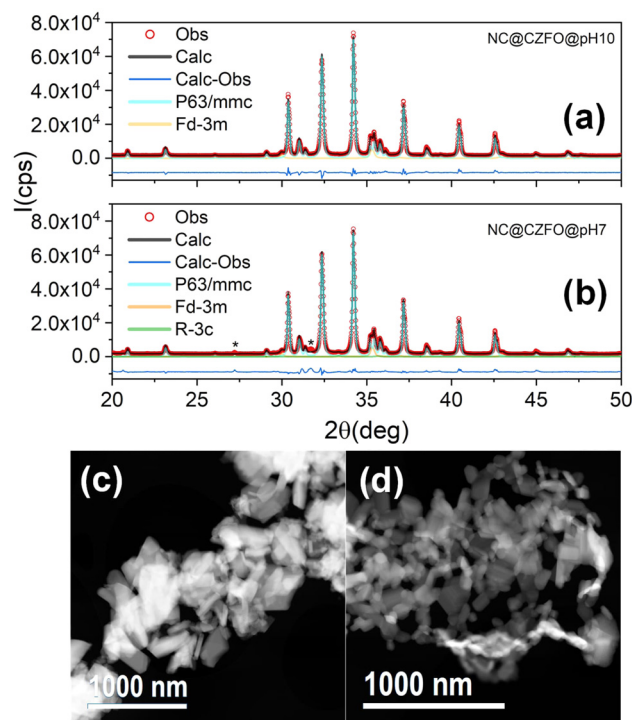

Fig. 3 Rietveld refinement analysis of the composites containing CZFO obtained at different pH for starting solutions: (a) pH = 10 (NC@CZFO@pH10) and (b) pH = 7 (NC@CZFO@pH10) For NC@CZFO@pH7, * indicate a possible impurity.[41] STEM-HAADF image of (c) NC@CZFO@pH7 and (d) NC@CZFO@pH10 showing the different sizes of the crystallites and their agglomeration.

phases for the composite at pH = 7 (NC@CZFO@pH7), which is inducing the independent growth of SFO. In contrast, a more homogeneous distribution of the CZFO phase prevents the growth of both phases, demonstrated earlier.[5,44,45] In addition, the presence of additional impurities, in the pattern at pH = 7,[41] suggests an incomplete growth of SFO.

The morphology of the composites has been investigated by STEM-HAADF revealing a perfect agreement with the XRPD results. In particular, Fig. 3(c) and (d) respectively show typical images of NC@CZFO@pH7 and NC@CZFO@pH10: the two nanocomposites are constituted by crystallites, strongly agglomerate in the sample obtained with pH = 7, while in that with pH = 10 they give rise to a more porous structure. Furthermore, comparing the two images, the crystallites in the pH = 7 composite are on average larger than in the pH = 10 one, as also evidenced by XRPD measurements. In such images, it is not easy to distinguish the spinel CZFO phase from the hexaferrite SFO one and for this reason, electron energy loss spectroscopy (EELS) measurements were performed in STEM mode to analyse the elemental distribution.

Two typical STEM-EELS compositional maps are reported in Fig. 4. In particular, in the top panel of Fig. 4 the composition of the NC@CZFO@pH7 sample is shown, and in the bottom panel of the same figure the composition of NC@CZFO@pH10 is reported. In both images it is possible to clearly distinguish CZFO and SFO structures, observing that in NC@CZFO@pH7

27820 | Phys. Chem. Chem. Phys., 2023, **25**, 27817–27828

This journal is © the Owner Societies 2023

Table 2 List of parameters: starting precursors' solution pH; lattice parameters a, b and c and crystallite sizes d for hexagonal and spinel ferrites extracted by XRPD analysis; compositional analysis by XRF; corresponding saturation at 5T (M_S^{5T}), and reduced remanent (M_R/M_S^{5T}) magnetization, coercive field ($\mu_0 H_C$) and switching/coercive fields ratio (H_{SW}/H_C) measured at 300 K and 5 K (in square brackets). *indicates the presence of an impurity (see main text for details)

| Sample | pH | Hexagonal | | | Spinel | | | 300 K [5 K] | | | |
		$a = b$; c (Å)	d_{ab}; d_c (nm)	wt% (XRF)	$a = b = c$ (Å)	d (nm)	wt% (XRF)	M_S^{5T} (A m^2 kg^{-1})	M_R/M_S^{5T}	$\mu_0 H_C$ (T)	H_{SW}/H_C
NC@CZFO@pH10	10	5.88047(2); 23.04622(5)	135(15); 107(10)	92.8(1)	8.4251(1)	32(4)	7.2(2)	73(1) [108(3)]	0.48(1) [0.50(1)]	0.48(2) [0.38(2)]	1.13 [1.10]
NC@CZFO@pH7	7	5.88118(2); 23.04327(6)	166(28); 116(10)	93.1(9)*	8.42248(2)	57(5)	6.9(3)*	64(1) [89(1)]	0.48(1) [0.49(1)]	0.51(3) [0.39(2)]	1.20 [1.22]
SFO@pH10	10	5.87879(2); 23.05107(5)	136(9); 114(5)	100	—	—	—	69(1) [100(3)]	0.49(1) [0.50(1)]	0.61(3) [0.51(3)]	1.09 [1.23]
NC@CFO@pH10	10	5.88073(2); 23.04259(5)	116(13); 92(8)	91.5(9)*	8.40204(6)	36(2)	8.5(8)*	69(1) [89(1)]	0.46(1) [0.50(1)]	0.55(3) [0.53(3)]	1.21 [1.26]

the CZFO is in partial contact with the SFO, while in the NC@CZFO@pH10 the CZFO is fully embedded in the SFO. The latter ensures an optimal connection between the two structures and consequently an excellent magnetic coupling. Furthermore, looking at the CZFO size, a reduced particle dimension of this phase is observed in pH = 10 ($\sim$35 nm) compared to pH = 7 ($\sim$100 nm) in agreement with XRPD measurements and with the effect of pH on the tendency of CZFO seeds to agglomerate.

Indeed, as a further confirmation of the particle size's change, the Mössbauer spectrum of NC@CZFO@pH10 recorded at 300 K (in Fig. 5(a)) displays overlapping mixed sextets due to SFO/CZFO particles with long relaxation time compared to the timescale of the technique (i.e., blocked particles),[46] but also a doublet due to a fraction of CZFO with shorter relaxation times, whose relative area decreases upon decreasing temperature (see Fig. 5(b) and Section 8.4 of ESI†). In contrast, the spectra of NC@CZFO@pH7 at both 300 and

77 K do not show any such doublet (Fig. 5(c) and (d)), as a result of high degree of agglomeration.

The Rietveld analysis does not show any secondary impurity upon introduction of Zn^{2+} in the spinel-structure of CZFO, while the (a) lattice parameter increases, as expected for similar Zn-doped particles, up to 8.4091 Å (see Section 8 of ESI†).[26,47] However, the annealing step in air for the composites might induce a cationic redistribution, as hinted by the change of lattice parameter (up to 8.4162 Å):[48–50] this is also in agreement with the observed segregation of hematite for a reference CZFO sample, whose resulting weight fraction ($\sim$11 wt%) after annealing matches with the iron excess determined by ICP ($\sim$13 wt%). Interestingly, the extracted lattice parameter for the CZFO phase in the composite increases even slightly further (up to $\sim$8.4251 and 8.4225 Å at pH = 10 and 7, respectively) (see ESI,† Section 8.3 for details). This increase in the composite might be due to Sr^{2+} substituting cations (Co^{2+} or Zn^{2+}) at the interface with the spinel phase. Previous studies have observed that the addition of Sr^{2+} in CFO and CZFO nanoparticles can increase the lattice parameter,[51,52] up to $\sim$8.42 Å for Sr^{2+} contents as low as 0.01 (1%) in CZFO samples with Co^{2+}/Zn^{2+} composition close to our case (e.g., Co$_{0.59}$Zn$_{0.4}$Sr$_{0.01}$Fe$_2$O$_4$). Additional strain effects induced by the contact between the two phases cannot be excluded.

Magnetic coupling

Fig. 6 shows the loops field dependence of magnetization of the nanocomposites, obtained at different pH, at T = 300 (a) and 5 K (b). The main parameters extracted from the loops (saturation magnetization, M_S, reduced magnetization, M_R/M_S, coercive field, H_C, and switching/coercive fields ratio, H_{SW}/H_C) are shown in Table 2. The loops show rather similar hysteretic behaviour, with a similar evolution of the coercivity as a function of temperature, which preserves large coercivities at 300 K, thus reflecting the dominant character of SFO over CZFO (SFO has an average size corresponding to a high coercivity range), with slight variations presumably due to the morphological differences together with the different size distributions of CZFO phase.

Besides, some significant differences may be noticed: the remanent magnetization from direct current demagnetization
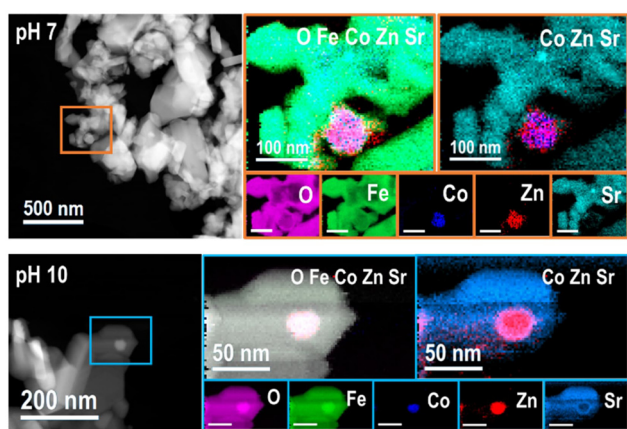

Fig. 4 Left: STEM-HAADF images of NC@CZFO@pH7 (top panel) and NC@CZFO@pH10 (bottom panel) nanocomposites showing the size and distribution of the CZFO phase with respect to the SFO one. Right panels: SEM-EELS maps showing all elements, all cations but Fe, and the individual O K-edge at 532 eV (pink), Fe L-edge at 708 eV (green), Co L-edge at 779 eV (blue), Zn L-edge at 1020 eV (red) and Sr L-edge at 1940 eV (light blue) (scale bars = 100 nm for NC@CZFO@pH7; scale bars = 50 nm for NC@CZFO@pH10).
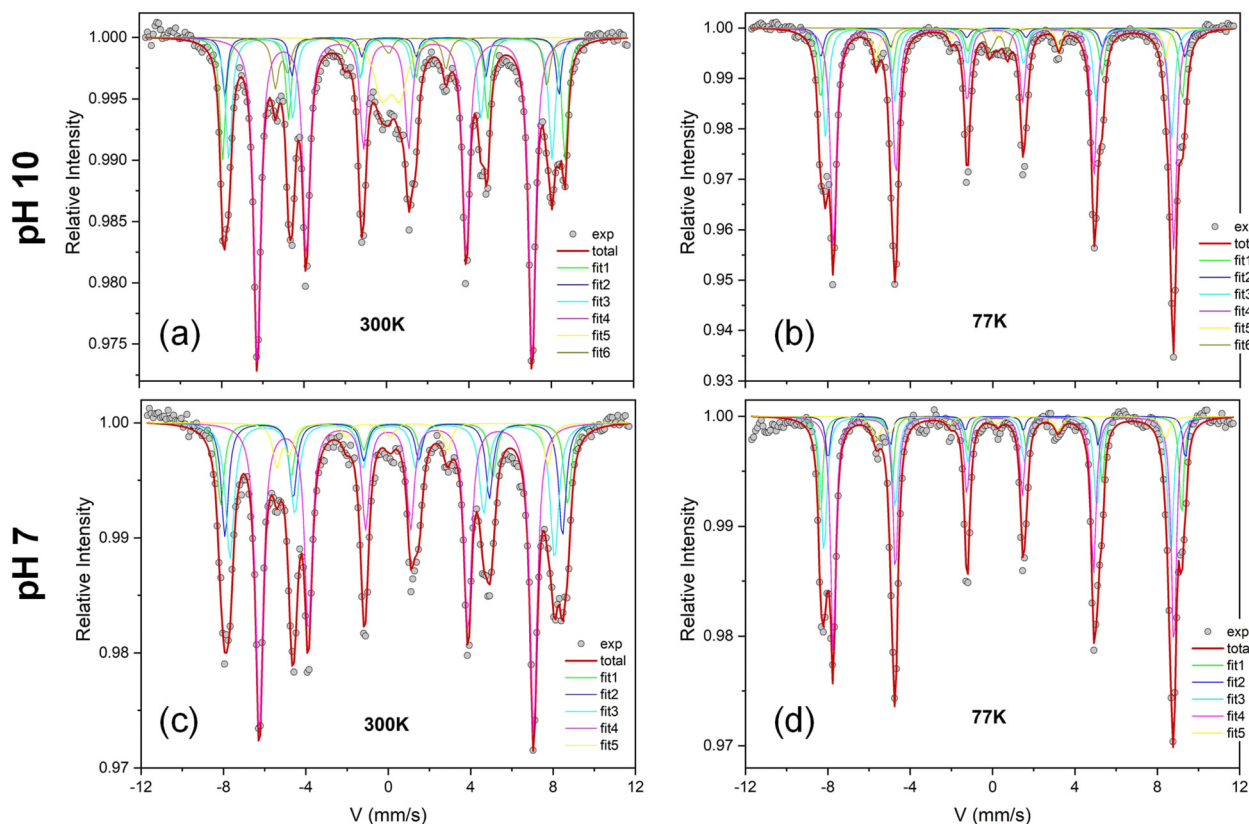
Fig. 5 Mössbauer spectra of NC@CZFO@pH10 at 300 K and 77 K (a), (b) and of NC@CZFO@pH7 at 300 K and 77 K (c), (d), respectively.

(DCD) experiments, M_{DCD}, *versus* reverse magnetic field,[53] at pH = 7 (NC@CZFO@pH7) is crossing the field axis at values H_{SW} (*i.e.* switching field) larger than H_C (at both 300 and 5 K) in comparison to pH = 10, hinting at the presence of irreversible phenomena due to the less uniform particle distribution. This can be confirmed by comparing the respective differentiated curve of M_{DCD} with respect to H, *i.e.* switching field distributions (SFDs) which represent the irreversible component of the susceptibility (χ_{irr}) (inset of Fig. 5): the relative difference (($H_{SW} - H_C$)/H_C) corresponds to 22% for NC@CZFO@pH7, compared to 10% for NC@CZFO@pH10, as may be generally observed for NPs systems.[54] On the other hand, the harder magnetic SFO phase dominates the reversal of NC@CZFO@pH10, pointing out its role in preventing the demagnetization of the softer Zn-doped ferrite. We also point out that the irreversible component accounts for the thermally blocked NPs, so some discrepancies may arise from the different timescales in the relaxation process.[55] The narrow and symmetric average SFD of NC@CZFO@pH10 suggests that the magnetic interaction here (whether or not direct exchange, *i.e.* dipolar-like) seems to be maximized in that system. The asymmetric SFDs of NC@CZFO@pH7 suggest the presence of more magnetic components at play.[56] In addition, the average size of CZFO in NC@CZFO@pH7 is close to the single domain limit, above which the magnetization does not reverse through a uniform coherent rotation (with the corresponding non-monotonic dependence of H_C with size, observed at low temperature for the annealed CZFO, see Fig. S19, ESI†).[57,58] Thus, the

enhancement of remanent magnetization for NC@CZFO@pH10 (~13%) in comparison to NC@CZFO@pH7, can be ascribed to the more homogenous distribution of CZFO in the host SFO, due to the higher colloidal stability at pH = 10, which maximize the magnetic coupling between the two phases, as a result of the controlled increase of surface area at the interface.[54]

However, understanding the coupling mechanisms in this kind of sintered magnets is a nontrivial task: such an effect might be hidden at room temperature, where the predominant harder magnetic nature of the Sr ferrite could mask the reversal of the small fraction of seeds. It was shown that a coupled system at room temperature might actually display features of a decoupled one at lower ones.[59] To better highlight the presence of an enhanced magnetic coupling between the two phases in NC@CZFO@pH10, owing to the optimized interfaces, we compare in Fig. 6(c) and (d) the hysteresis loops at 300 and 5 K for the weighted sum (*i.e.*, superposition)of SFO@pH10 and annealed CZFO seeds (with the corresponding weight ratio), and the experimental loops for NC@CZFO@pH10 as a reference. We should keep in mind that we expect the anisotropy of CZFO to increase as temperature is lowered, while the anisotropy of SFO decreases,[60] and thus the critical size for effective coupling changes significantly.[61] Even if CZFO phases grow differently whether in the composite or individually (see Section 8 of ESI†), at 5 K it is evident (despite the low concentration of CZFO, 7 wt%) that the hysteresis for the superposition shows a double-loop response, typical of mixtures/phase-segregated
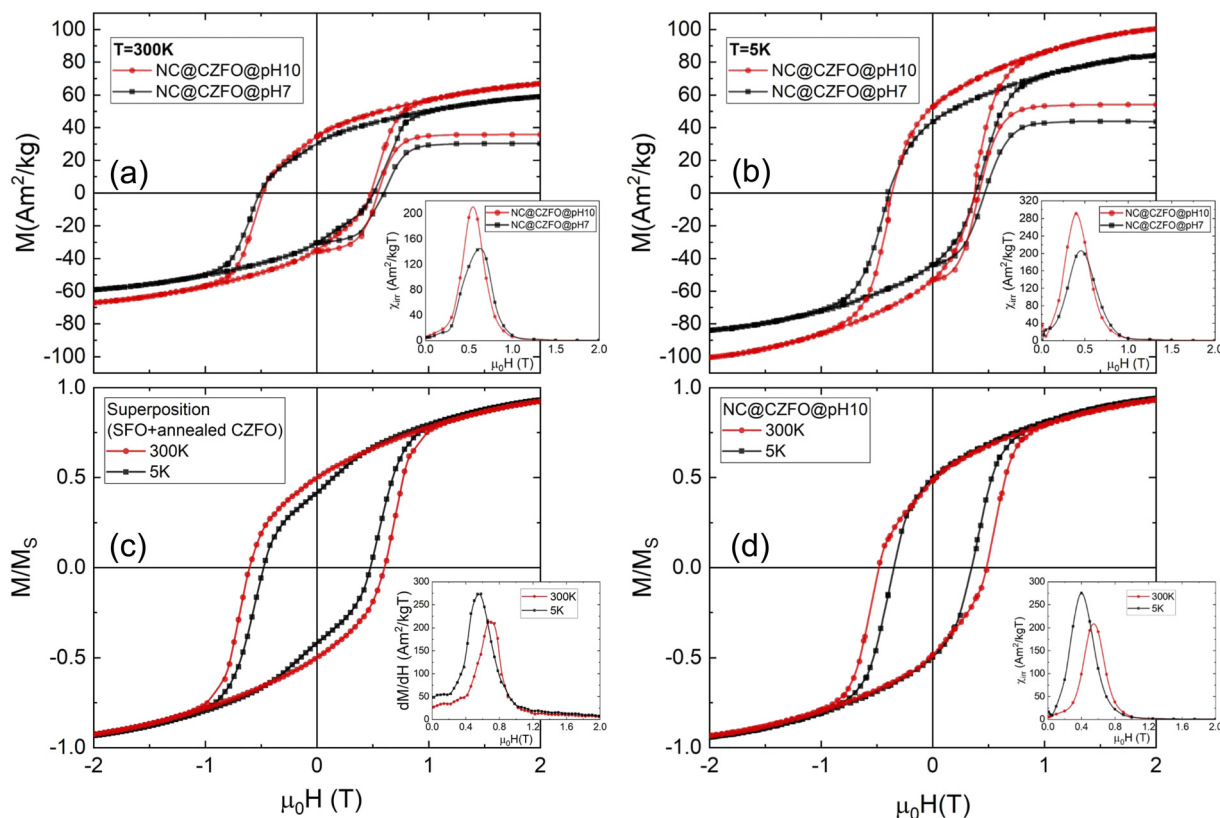
27822 | *Phys. Chem. Chem. Phys.*, 2023, **25**, 27817–27828

This journal is © the Owner Societies 2023

Fig. 6 Magnetization M vs. magnetic field $\mu_0 H$ curves for NC@CZFO@pH10 and NC@CZFO@pH7 and magnetization M_{DCD} vs. reverse magnetic field H curves for the corresponding samples at (a) 300 K and (b) 5 K. In the insets, the associated SFDs. Normalized magnetization M vs. magnetic field $\mu_0 H$ curves for (c) superposition of CZFO (annealed at the desired temperature) and SFO@pH10 and (d) NC@CZFO@pH10, at both 300 and 5 K. In the insets, the corresponding switching field distributions.

systems.[5,17] On the contrary, the composite shows an ordinary single-loop response at low temperatures, as a result of strong magnetic interactions between the NPs. Interestingly, we point out that at 300 K even hysteresis curve for the superposition (where no magnetic interactions are considered) displays a single loop, demonstrating the need of low-temperature measurement to fully characterize the reversal in those binary systems.[61]

Effect of elemental doping on the anisotropy of NCs

In the previous section we have shown that the magnetic coupling between CZFO and the matrix can be tuned by the effect of the initial partial agglomeration. To evaluate the role of anisotropy of the seed phase on the overall composite magnetic behaviour, undoped Co–ferrite (CFO) NPs with the same size (6(1) nm) were synthesized using the same route and used to prepare a composite (NC@CFO@pH10) at pH = 10 starting conditions. XRPD analysis revealed a CFO phase of 36(2) nm, thus confirming the robustness of the pH-controlled agglomeration, as observed for NC@CZFO@pH10. Lattice parameters for SFO@pH10 are in good agreement with the other composites, while for CFO do not change significantly (see ESI†). The only difference is the small hematite impurity accompanied by unreacted $SrCO_3$ which resulted in a slightly lower SFO fraction (and in turn a larger CFO weight fraction (~ 8.5 wt%) as shown

by XRF in ESI†). Nonetheless, our purpose here is to show that the strength of magnetic coupling, qualitatively evinced by demagnetization experiments, can be evaluated from the correlation between the change of magnetic anisotropy of composite and that of the seeds.

As shown in Fig. 7, the anisotropy of the composite changes according to the anisotropy of the corresponding spinel phase. At both 300 K and 5 K, the coercive field of NC@CFO@pH10 increases as expected for regular undoped CFO particles, while the saturation magnetization decreases. These results are confirming earlier observations reported in ref. 54 and 62. In the insets of Fig. 7, we note that the average switching field of NC@CFO@pH10 is located at lower values than that of NC@CFO@pH10, as the corresponding magnetic anisotropy of CZFO is lower than that of CFO,[25] thus highlighting the effective tuning of the magnetic anisotropy of the composite.[27] The effective magnetic anisotropy of the composites is calculated in the Section 8.5 of the ESI.† Interestingly, a much higher value is obtained for NC@CFO@pH10 at 5 K, suggesting a strong effect produced by the CFO seeds, as also indicated by the small secondary peak of the irreversible susceptibility at large fields ($\mu_0 H_{SW} \sim 1.2$T).[54] Indeed, the corresponding anisotropy field for non-agglomerated (smaller) particles is much larger. As also previously evidenced by Mössbauer spectrometry for the NC@CZFO@pH10 case, we may expect to have smaller
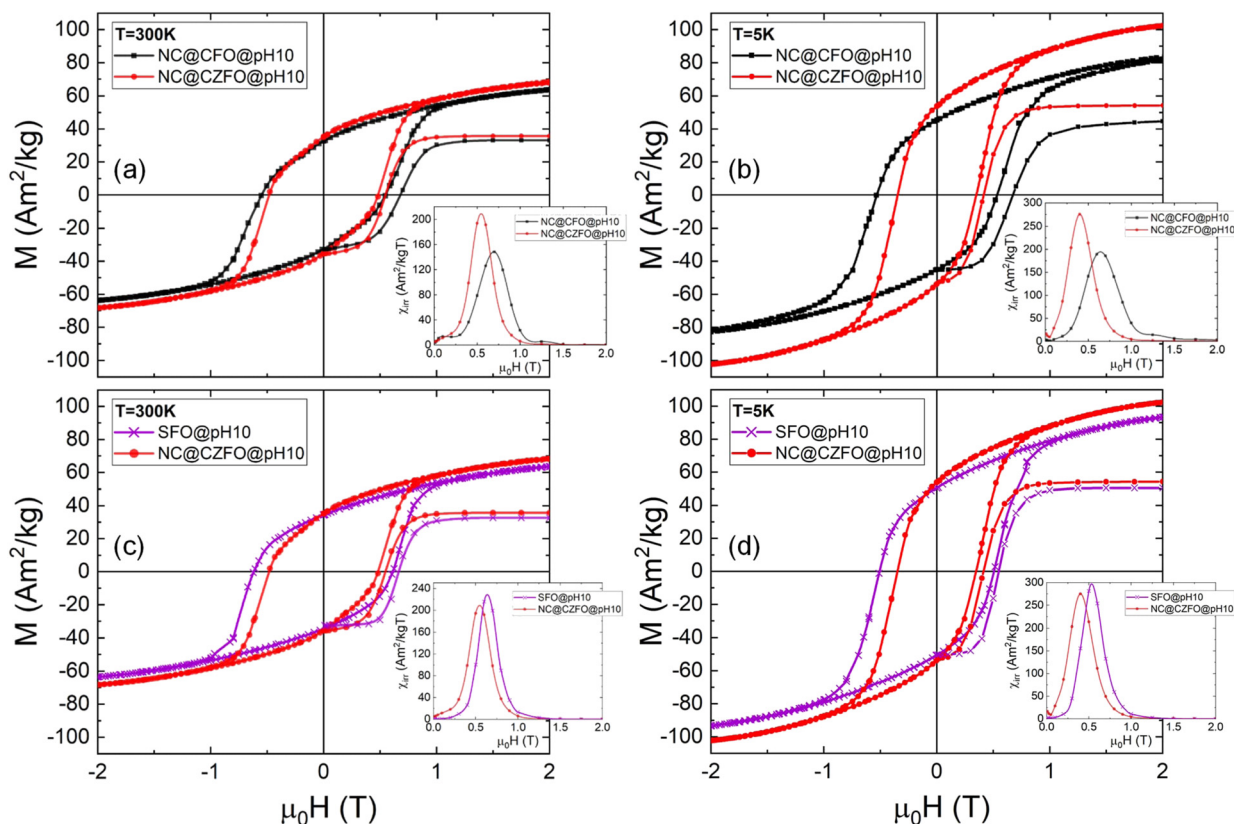
This journal is © the Owner Societies 2023

Phys. Chem. Chem. Phys., 2023, **25**, 27817–27828 | **27823**

Fig. 7 Magnetization M vs. magnetic field μ_0H curves for nanocomposites with preformed CFO and CZFO NPs at pH = 10 (NC@CFO@pH10 and NC@CZFO@pH10) and magnetization M_{DCD} vs. reverse magnetic field H curves for the corresponding samples at (a) 300 K and (b) 5 K. For comparison, panels for SFO synthesized at pH = 10 (SFO@pH10), and NC@CZFO@pH10 are reported at (c) 300 K and (d) 5 K.

particles for NC@CFO@pH10 as well (owing to the colloidal stability at pH = 10) that are not coupled with the matrix and thus magnetically reverse independently (inset of Fig. 7(b)), since we observed a doublet assigned to the CZFO component in the spectrum at 300 K, which drastically decreases at 77 K (*i.e.* moving from thermally unblocked to blocked). In contrast, such contribution is hidden for CZFO, as the magnetic anisotropy is expected to be lower. We should point out that K_{eff} considered here is used to compare the anisotropy for the composites.

Furthermore, by comparing the M_{DCD} curves, we point out that remarkably, a slight increase of remanence is produced for NC@CZFO@pH10 compared to NC@CFO@pH10, revealing the possibility to enhance the remanence by coupling SFO to a second prototypical particle, extremely important for technological applications, such as permanent magnets.[63–66] Among other synthesis methods to produce composites with similar magnetic properties (see Section 9 of ESI†),[67–69] this design is essentially suitable for any type of particle, thus opening up the way for potential application of this pH-controlled agglomeration in other systems.

Conclusions

We have designed a seed-mediated approach to synthesize bimagnetic composites by controlling the aggregation of the

preformed NPs *via* control over the colloidal stability inside a magnetically hard matrix. The nanocrystallites' sizes extracted from XRPD analysis match the results from STEM-EELS compositional maps, which evidence the inclusion of the NPs in the SFO. The observed enhancement of remanent magnetization for NC@CZFO@pH10 is related to the homogenous distribution of NPs in the composite, which favours a higher degree of magnetic interactions between the two phases in contact (*i.e.*, an increase of surface area at the interface). Furthermore, we demonstrate that the change of magnetic anisotropy in the seed (*i.e.*, CZFO) is extended to the composites, since their anisotropy changes accordingly. To conclude, we propose a simple synthetic route to obtain nanomaterials with controlled structural and well-defined morphological properties.

Author contributions

27824 | *Phys. Chem. Chem. Phys.*, 2023, **25**, 27817–27828

This journal is © the Owner Societies 2023

contributed to the results discussion and revision of the article, which was written mainly by P. M. and R. M.

Conflicts of interest

There are no conflicts to declare.

Acknowledgements

References

1 A. Chen, Q. Su, H. Han, E. Enriquez and Q. Jia, Metal Oxide Nanocomposites: A Perspective from Strain, Defect, and Interface, *Adv. Mater.*, 2019, **31**(4), 1803241, DOI: **10.1002/adma.201803241**.

2 S. E. Shirsath, M. H. N. Assadi, J. Zhang, N. Kumar, A. S. Gaikwad, J. Yang, H. E. Maynard-Casely, Y. Y. Tay, J. Du, H. Wang, Y. Yao, Z. Chen, J. Zhang, S. Zhang, S. Li and D. Wang, Interface-Driven Multiferroicity in Cubic BaTiO$_3$–SrTiO$_3$ Nanocomposites, *ACS Nano*, 2022, **16**(9), 15413–15424, DOI: **10.1021/acsnano.2c07215**.

3 A. Wang, Y. Dou, X. Yang, Q. Wang, M. S. Sudi, L. Zhao, D. Shang, W. Zhu and J. Ren, Efficient Oxygen Evolution Reaction from Iron-Molybdenum Nitride/Molybdenum Oxide Heterostructured Composites, *Dalton Trans.*, 2023, **52**(32), 11234–11242, DOI: **10.1039/D3DT01295F**.

4 G. Zhang, J. Chen, Z. Zhang, M. Sun, Y. Yu, J. Wang and S. Cai, A Novel Parametric Model for Nonlinear Hysteretic Behaviours with Strain-Stiffening of Magnetorheological Gel Composite, *Compos. Struct.*, 2023, **318**, 117082, DOI: **10.1016/j.compstruct.2023.117082**.

5 G. Muscas, P. Anil Kumar, G. Barucca, G. Concas, G. Varvaro, R. Mathieu and D. Peddis, Designing New Ferrite/Manganite Nanocomposites, *Nanoscale*, 2016, **8**(4), 2081–2089, DOI: **10.1039/C5NR07572F**.

6 E. F. Kneller and R. Hawig, The Exchange-Spring Magnet: A New Material Principle for Permanent Magnets, *IEEE Trans. Magn.*, 1991, **27**(4), 3588–3560, DOI: **10.1109/20.102931**.

7 J. Livage, M. Henry and C. Sanchez, Sol-Gel Chemistry of Transition Metal Oxides, *Prog. Solid State Chem.*, 1988, **18**(4), 259–341, DOI: **10.1016/0079-6786(88)90005-2**.

8 T. Ohya, M. Ito, K. Yamada, T. Ban, Y. Ohya and Y. Takahashi, Aqueous Titanate Sols from Ti Alkoxide-Hydroxycarboxylic Acid System and Preparation of Titania Films from the Sols, *J. Sol-Gel Sci. Technol.*, 2004, **30**(2), 71–81, DOI: **10.1023/B:JSST.0000034694.61859.78**.

9 E. Scolan and C. Sanchez, Synthesis and Characterization of Surface-Protected Nanocrystalline Titania Particles, *Chem. Mater.*, 1998, **10**(10), 3217–3223, DOI: **10.1021/cm980322q**.

10 C. Cannas, A. Musinu, D. Peddis and G. Piccaluga, Synthesis and Characterization of CoFe$_2$O$_4$ Nanoparticles Dispersed in a Silica Matrix by a Sol–Gel Autocombustion Method, *Chem. Mater.*, 2006, **18**(16), 3835–3842, DOI: **10.1021/cm060650n**.

11 M. Zayat and D. Levy, Blue CoAl$_2$O$_4$ Particles Prepared by the Sol–Gel and Citrate–Gel Methods, *Chem. Mater.*, 2000, **12**(9), 2763–2769, DOI: **10.1021/cm001061z**.

12 R. C. Pullar, Hexagonal Ferrites: A Review of the Synthesis, Properties and Applications of Hexaferrite Ceramics, *Prog. Mater. Sci.*, 2012, **57**(7), 1191–1334, DOI: **10.1016/j.pmatsci.2012.04.001**.

13 A. Z. Eikeland, M. Stingaciu, A. H. Mamakhel, M. Saura-Múzquiz and M. Christensen, Enhancement of Magnetic Properties through Morphology Control of SrFe$_{12}$O$_{19}$ Nanocrystallites, *Sci. Rep.*, 2018, **8**(1), 7325, DOI: **10.1038/s41598-018-25662-8**.

14 C. Cannas, A. Falqui, A. Musinu, D. Peddis and G. Piccaluga, CoFe$_2$O$_4$ Nanocrystalline Powders Prepared by Citrate-Gel Methods: Synthesis, Structure and Magnetic Properties, *J. Nanoparticle Res.*, 2006, **8**(2), 255–267, DOI: **10.1007/s11051-005-9028-7**.

15 M. Andrés Vergés, R. Costo, A. G. Roca, J. F. Marco, G. F. Goya, C. J. Serna and M. P. Morales, Uniform and Water Stable Magnetite Nanoparticles with Diameters around the Monodomain–Multidomain Limit, *J. Phys. D: Appl. Phys.*, 2008, **41**(13), 134003, DOI: **10.1088/0022-3727/41/13/134003**.

16 P. Guardia, N. Pérez, A. Labarta and X. Batlle, Controlled Synthesis of Iron Oxide Nanoparticles over a Wide Size Range, *Langmuir*, 2010, **26**(8), 5843–5847, DOI: **10.1021/la903767e**.

17 H. Zeng, J. Li, J. P. Liu, Z. L. Wang and S. Sun, Exchange-Coupled Nanocomposite Magnets by Nanoparticle Self-Assembly, *Nature*, 2002, **420**(6914), 395–398, DOI: **10.1038/nature01208**.

18 E. H. Sánchez, M. Vasilakaki, S. S. Lee, P. S. Normile, G. Muscas, M. Murgia, M. S. Andersson, G. Singh, R. Mathieu, P. Nordblad, P. C. Ricci, D. Peddis, K. N. Trohidou, J. Nogués and J. A. De Toro, Simultaneous Individual and Dipolar Collective Properties in Binary Assemblies of Magnetic Nanoparticles, *Chem. Mater.*, 2020, **32**(3), 969–981, DOI: **10.1021/acs.chemmater.9b03268**.

19 B. Balasubramanian, B. Das, R. Skomski, W. Y. Zhang and D. J. Sellmyer, Novel Nanostructured Rare-Earth-Free Magnetic Materials with High Energy Products, *Adv. Mater.*, 2013, **25**(42), 6090–6093, DOI: **10.1002/adma.201302704**.

20 S. E. Shirsath, X. Liu, M. H. N. Assadi, A. Younis, Y. Yasukawa, S. K. Karan, J. Zhang, J. Kim, D. Wang,

This journal is © the Owner Societies 2023

Phys. Chem. Chem. Phys., 2023, **25**, 27817–27828 | 27825

A. Morisako, Y. Yamauchi and S. Li, Au Quantum Dots Engineered Room Temperature Crystallization and Magnetic Anisotropy in $CoFe_2O_4$ Thin Films, *Nanoscale Horiz.*, 2019, **4**(2), 434–444, DOI: **10.1039/C8NH00278A**.

21 R. A. Pawar, S. M. Patange, A. R. Shitre, S. K. Gore, S. S. Jadhav and S. E. Shirsath, Crystal Chemistry and Single-Phase Synthesis of Gd^{3+} Substituted Co–Zn Ferrite Nanoparticles for Enhanced Magnetic Properties, *RSC Adv.*, 2018, **8**(44), 25258–25267, DOI: **10.1039/C8RA04282A**.

22 S. E. Shirsath, R. H. Kadam, K. M. Batoo, D. Wang and S. Li, Co–Al-Substituted Strontium Hexaferrite for Rare Earth Free Permanent Magnet and Microwave Absorber Application, *J. Phys. D: Appl. Phys.*, 2021, **54**(2), 024001, DOI: **10.1088/1361-6463/abb9d5**.

23 G. Muscas, N. Yaacoub, G. Concas, F. Sayed, R. Sayed Hassan, J. M. Greneche, C. Cannas, A. Musinu, V. Foglietti, S. Casciardi, C. Sangregorio and D. Peddis, Evolution of the Magnetic Structure with Chemical Composition in Spinel Iron Oxide Nanoparticles, *Nanoscale*, 2015, **7**(32), 13576–13585, DOI: **10.1039/C5NR02723C**.

24 A. Ghasemi, A. Paesano, C. F. Cerqueira Machado, S. E. Shirsath, X. Liu and A. Morisako, Mössbauer Spectroscopy, Magnetic Characteristics, and Reflection Loss Analysis of Nickel-Strontium Substituted Cobalt Ferrite Nanoparticles, *J. Appl. Phys.*, 2014, **115**(17), 17A522, DOI: **10.1063/1.4866232**.

25 M. Baričić, P. Maltoni, G. Barucca, N. Yaacoub, F. Canepa, R. Mathieu and D. Peddis, Correlation between Magnetic Properties and Composition/Cationic Distribution of Spinel Ferrite Nanoparticles upon Substitution by Ni^{2+} and Zn^{2+} (In Manuscript).

26 M. Albino, E. Fantechi, C. Innocenti, A. López-Ortega, V. Bonanni, G. Campo, F. Pineider, M. Gurioli, P. Arosio, T. Orlando, G. Bertoni, C. de Julián Fernández, A. Lascialfari and C. Sangregorio, Role of Zn^{2+} Substitution on the Magnetic, Hyperthermic, and Relaxometric Properties of Cobalt Ferrite Nanoparticles, *J. Phys. Chem. C*, 2019, **123**(10), 6148–6157, DOI: **10.1021/acs.jpcc.8b10998**.

27 V. Mameli, A. Musinu, A. Ardu, G. Ennas, D. Peddis, D. Niznansky, C. Sangregorio, C. Innocenti, N. T. K. Thanh and C. Cannas, Studying the Effect of Zn-Substitution on the Magnetic and Hyperthermic Properties of Cobalt Ferrite Nanoparticles, *Nanoscale*, 2016, **8**(19), 10124–10137, DOI: **10.1039/C6NR01303A**.

28 P. Maltoni, T. Sarkar, G. Varvaro, G. Barucca, S. A. Ivanov, D. Peddis and R. Mathieu, Towards Bi-Magnetic Nanocomposites as Permanent Magnets through the Optimization of the Synthesis and Magnetic Properties of $SrFe_{12}O_{19}$ Nanocrystallites, *J. Phys. D: Appl. Phys.*, 2021, **54**(12), 124004, DOI: **10.1088/1361-6463/abd20d**.

29 M. Iacomino, J. I. Paez, R. Avolio, A. Carpentieri, L. Panzella, G. Falco, E. Pizzo, M. E. Errico, A. Napolitano, A. del Campo and M. D'Ischia, Multifunctional Thin Films and Coatings from Caffeic Acid and a Cross-Linking Diamine, *Langmuir*, 2017, **33**(9), 2096–2102, DOI: **10.1021/acs.langmuir.6b04079**.

30 A. Plan Sangnier, A. B. Van de Walle, A. Curcio, R. Le Borgne, L. Motte, Y. Lalatonne and C. Wilhelm, Impact of Magnetic Nanoparticle Surface Coating on Their Long-Term Intracellular Biodegradation in Stem Cells, *Nanoscale*, 2019, **11**(35), 16488–16498, DOI: **10.1039/C9NR05624F**.

31 Y. Xu, Y. Ma, S. Xu, G. Zheng and Z. Dai, Diluted and Undiluted Monodispersed $CoFe_2O_4$ Nanoparticles: The Effects of Post-Annealing on Magnetic Properties, *J. Mater. Sci.*, 2015, **50**(13), 4486–4494, DOI: **10.1007/s10853-015-8997-x**.

32 F. Borges, J. L. F. C. Lima, I. Pinto, S. Reis and C. Siquet, Application of a Potentiometric System with Data-Analysis Computer Programs to the Quantification of Metal-Chelating Activity of Two Natural Antioxidants: Caffeic Acid and Ferulic Acid, *Helv. Chim. Acta*, 2003, **86**(9), 3081–3087, DOI: **10.1002/hlca.200390250**.

33 S. Sun, H. Zeng, D. B. Robinson, S. Raoux, P. M. Rice, S. X. Wang and G. Li, Monodisperse MFe_2O_4 (M = Fe, Co, Mn) Nanoparticles, *J. Am. Chem. Soc.*, 2004, **126**(1), 273–279, DOI: **10.1021/ja0380852**.

34 S. Slimani, A. Talone, M. Abdolrahimi, P. Imperatori, G. Barucca, D. Fiorani and D. Peddis, Morpho-Structural and Magnetic Properties of $CoFe_2O_4/SiO_2$ Nanocomposites: The Effect of the Molecular Coating, *J. Phys. Chem. C*, 2023, **127**(18), 8840–8849, DOI: **10.1021/acs.jpcc.3c01252**.

35 J. Rodríguez-Carvajal, Recent Advances in Magnetic Structure Determination by Neutron Powder Diffraction, *Phys. B*, 1993, **192**(1–2), 55–69, DOI: **10.1016/0921-4526(93)90108-I**.

36 P. Vaqueiro and M. A. López-Quintela, Influence of Complexing Agents and pH on Yttrium–Iron Garnet Synthesized by the Sol–Gel Method, *Chem. Mater.*, 1997, **9**(12), 2836–2841, DOI: **10.1021/cm970165f**.

37 A. E. Danks, S. R. Hall and Z. Schnepp, The Evolution of 'Sol–Gel' Chemistry as a Technique for Materials Synthesis, *Mater. Horiz.*, 2016, **3**(2), 91–112, DOI: **10.1039/C5MH00260E**.

38 F. Borges, C. Guimaraes, J. Lima, I. Pinto and S. Reis, Potentiometric Studies on the Complexation of Copper(II) by Phenolic Acids as Discrete Ligand Models of Humic Substances, *Talanta*, 2005, **66**(3), 670–673, DOI: **10.1016/j.talanta.2004.12.012**.

39 K. V. Korpany, D. D. Majewski, C. T. Chiu, S. N. Cross and A. S. Blum, Iron Oxide Surface Chemistry: Effect of Chemical Structure on Binding in Benzoic Acid and Catechol Derivatives, *Langmuir*, 2017, **33**(12), 3000–3013, DOI: **10.1021/acs.langmuir.6b03491**.

40 J. Lim, S. P. Yeap, H. X. Che and S. C. Low, Characterization of Magnetic Nanoparticle by Dynamic Light Scattering, *Nanoscale Res. Lett.*, 2013, **8**(1), 381, DOI: **10.1186/1556-276X-8-381**.

41 H. Vijayan, C. G. Knudsen, M. I. Mørch and M. Christensen, Ultrathin Nanoplatelets of Six-Line Ferrihydrite Enhances the Magnetic Properties of Hexaferrite, *Mater. Chem. Front.*, 2021, **5**(9), 3699–3709, DOI: **10.1039/D1QM00224D**.

42 T. T. V. Nga, N. P. Duong, T. T. Loan and T. D. Hien, Key Step in the Synthesis of Ultrafine Strontium Ferrite Powders ($SrFe_{12}O_{19}$) by Sol–Gel Method, *J. Alloys Compd.*, 2014, **610**, 630–634, DOI: **10.1016/j.jallcom.2014.04.193**.

43 H.-F. Yu and K.-C. Huang, Effects of PH and Citric Acid Contents on Characteristics of Ester-Derived $BaFe_{12}O_{19}$

27826 | *Phys. Chem. Chem. Phys.*, 2023, **25**, 27817–27828

This journal is © the Owner Societies 2023

Powder, *J. Magn. Magn. Mater.*, 2003, **260**(3), 455–461, DOI: **10.1016/S0304-8853(02)01389-6**.

44 P. Maltoni, T. Sarkar, G. Barucca, G. Varvaro, F. Locardi, D. Peddis and R. Mathieu, Tuning the Magnetic Properties of Hard–Soft $SrFe_{12}O_{19}/CoFe_2O_4$ Nanostructures *via* Composition/Interphase Coupling, *J. Phys. Chem. C*, 2021, **125**(10), 5927–5936, DOI: **10.1021/acs.jpcc.1c00355**.

45 F. Sayed, G. Kotnana, G. Muscas, F. Locardi, A. Comite, G. Varvaro, D. Peddis, G. Barucca, R. Mathieu and T. Sarkar, Symbiotic, Low-Temperature, and Scalable Synthesis of Bi-Magnetic Complex Oxide Nanocomposites, *Nanoscale Adv.*, 2020, **2**(2), 851–859, DOI: **10.1039/C9NA00619B**.

46 M. F. Hansen, F. Bødker, S. Mørup, C. Djurberg and P. Svedlindh, Magnetic Properties of Non-Interacting Fe–C Nanoparticles, *J. Magn. Magn. Mater.*, 1998, **177–181**, 928–930, DOI: **10.1016/S0304-8853(97)00751-8**.

47 H. L. Andersen, C. Granados-Miralles, M. Saura-Múzquiz, M. Stingaciu, J. Larsen, F. Søndergaard-Pedersen, J. V. Ahlburg, L. Keller, C. Frandsen and M. Christensen, Enhanced Intrinsic Saturation Magnetization of $Zn_xCo_{1−x}Fe_2O_4$ Nanocrystallites with Metastable Spinel Inversion, *Mater. Chem. Front.*, 2019, **3**(4), 668–679, DOI: **10.1039/C9QM00012G**.

48 J. Hölscher, M. Petrecca, M. Albino, P. G. Garbus, M. Saura-Múzquiz, C. Sangregorio and M. Christensen, Magnetic Property Enhancement of Spinel Mn–Zn Ferrite through Atomic Structure Control, *Inorg. Chem.*, 2020, **59**(15), 11184–11192, DOI: **10.1021/acs.inorgchem.0c01809**.

49 L. Tung, V. Kolesnichenko, G. Caruntu, D. Caruntu, Y. Remond, V. Golub, C. O'Connor and L. Spinu, Annealing Effects on the Magnetic Properties of Nanocrystalline Zinc Ferrite, *Phys. B*, 2002, **319**(1–4), 116–121, DOI: **10.1016/S0921-4526(02)01114-6**.

50 E. J. W. Verwey and E. L. Heilmann, Physical Properties and Cation Arrangement of Oxides with Spinel Structures I. Cation Arrangement in Spinels, *J. Chem. Phys.*, 1947, **15**(4), 174–180, DOI: **10.1063/1.1746464**.

51 R. Kumar and M. Kar, Lattice Strain Induced Magnetism in Substituted Nanocrystalline Cobalt Ferrite, *J. Magn. Magn. Mater.*, 2016, **416**, 335–341, DOI: **10.1016/j.jmmm.2016.05.035**.

52 P. Imanipour, S. Hasani, M. Afshari, S. Sheykh, A. Seifoddini and K. Jahanbani-Ardakani, The Effect of Divalent Ions of Zinc and Strontium Substitution on the Structural and Magnetic Properties on the Cobalt Site in Cobalt Ferrite, *J. Magn. Magn. Mater.*, 2020, **510**, 166941, DOI: **10.1016/j.jmmm.2020.166941**.

53 A. López-Ortega, M. Estrader, G. Salazar-Alvarez, A. G. Roca and J. Nogués, Applications of Exchange Coupled Bi-Magnetic Hard/Soft and Soft/Hard Magnetic Core/Shell Nanoparticles, *Phys. Rep.*, 2015, **553**, 1–32, DOI: **10.1016/j.physrep.2014.09.007**.

54 F. Sayed, G. Muscas, S. Jovanovic, G. Barucca, F. Locardi, G. Varvaro, D. Peddis, R. Mathieu and T. Sarkar, Controlling Magnetic Coupling in Bi-Magnetic Nanocomposites, *Nanoscale*, 2019, **11**(30), 14256–14265, DOI: **10.1039/C9NR05364F**.

55 A. Omelyanchik, M. Salvador, F. D'Orazio, V. Mameli, C. Cannas, D. Fiorani, A. Musinu, M. Rivas, V. Rodionova,

G. Varvaro and D. Peddis, Magnetocrystalline and Surface Anisotropy in $CoFe_2O_4$ Nanoparticles, *Nanomaterials*, 2020, **10**(7), 1288, DOI: **10.3390/nano10071288**.

56 P. Maltoni, G. Barucca, B. Rutkowski, M. C. Spadaro, P. E. Jönsson, G. Varvaro, N. Yaacoub, J. A. De Toro, D. Peddis and R. Mathieu, Unraveling Exchange Coupling in Ferrites Nano-Heterostructures, 2023, submitted.

57 M. Y. Rafique, L. Pan, Q. Javed, M. Z. Iqbal and L. Yang, Influence of $NaBH_4$ on the Size, Composition, and Magnetic Properties of $CoFe_2O_4$ Nanoparticles Synthesized by Hydrothermal Method, *J. Nanoparticle Res.*, 2012, **14**(10), 1189, DOI: **10.1007/s11051-012-1189-6**.

58 S. Okamoto, O. Kitakami, N. Kikuchi, T. Miyazaki, Y. Shimada and Y. K. Takahashi, Size Dependences of Magnetic Properties and Switching Behavior in FePt $L1_0$ Nanoparticles, *Phys. Rev. B: Condens. Matter Mater. Phys.*, 2003, **67**(9), 094422, DOI: **10.1103/PhysRevB.67.094422**.

59 J. P. Liu, R. Skomski, Y. Liu and D. J. Sellmyer, Temperature Dependence of Magnetic Hysteresis of RCo_x:Co Nanocomposites (R = Pr and Sm), *J. Appl. Phys.*, 2000, **87**(9), 6740–6742, DOI: **10.1063/1.372826**.

60 P. Maltoni, G. Varvaro, M. Abdolrahimi, D. Peddis and R. Mathieu, Time and Temperature Dependent Magnetic Viscosity Experiments on Sr/Co Nanoferrite Particles, *J. Appl. Phys.*, 2023, **133**(16), 163902, DOI: **10.1063/5.0144701**.

61 A. Quesada, C. Granados-Miralles, A. López-Ortega, S. Erokhin, E. Lottini, J. Pedrosa, A. Bollero, A. M. Aragón, F. Rubio-Marcos, M. Stingaciu, G. Bertoni, C. de Julián Fernández, C. Sangregorio, J. F. Fernández, D. Berkov and M. Christensen, Energy Product Enhancement in Imperfectly Exchange-Coupled Nanocomposite Magnets, *Adv. Electron. Mater.*, 2016, **2**(4), 1500365, DOI: **10.1002/aelm.201500365**.

62 P. Maltoni, T. Sarkar, G. Barucca, G. Varvaro, D. Peddis and R. Mathieu, Exploring the Magnetic Properties and Magnetic Coupling in $SrFe_{12}O_{19}/Co_{1−x}Zn_xFe_2O_4$ Nanocomposites, *J. Magn. Magn. Mater.*, 2021, **535**, 168095, DOI: **10.1016/j.jmmm.2021.168095**.

63 C. de Julian Fernandez, C. Sangregorio, J. de la Figuera, B. Belec, D. Makovec and A. Quesada, Topical Review: Progress and Prospects of Hard Hexaferrites for Permanent Magnet Applications, *J. Phys. D: Appl. Phys.*, 2021, **54**, 153001, DOI: **10.1088/1361-6463/abd272**.

64 D. Peddis, P. E. Jönsson, S. Laureti and G. Varvaro, Magnetic Interactions: A Tool to Modify the Magnetic Properties of Materials Based on Nanoparticles, in *Frontiers of Nanoscience*, ed. C. Binns, Elsevier, 2014, vol. 6, pp. 129–188, DOI: **10.1016/B978-0-08-098353-0.00004-X**.

65 M. A. Almessiere, Y. Slimani, A. V. Trukhanov, A. Sadaqat, A. D. Korkmaz, N. A. Algarou, H. Aydın, A. Baykal and M. S. Toprak, Review on Functional Bi-Component Nanocomposites Based on Hard/Soft Ferrites: Structural, Magnetic, Electrical and Microwave Absorption Properties, *Nano-Struct. Nano-Objects*, 2021, **26**, 100728, DOI: **10.1016/j.nanoso.2021.100728**.

66 O. T. L. Traistaru, P. Shyam, M. Christensen and S. P. Madsen, Optimizing the Energy Product of Exchange-

This journal is © the Owner Societies 2023

Phys. Chem. Chem. Phys., 2023, **25**, 27817–27828 | **27827**

Coupled Soft/Hard $Zn_{0.2}Fe_{2.8}O_4/SrFe_{12}O_{19}$ Magnets, *J. Appl. Phys.*, 2022, **132**(16), 163904, DOI: **10.1063/5.0103242**.

67 P. Shyam, M. Mørch, A. Z. Eikeland, J. Ahlburg, A. Mamakhel, M. Saura-Múzquiz and M. Christensen, Combined Characterization Approaches to Investigate Magnetostructural Effects in Exchange-Spring Ferrite Nanocomposite Magnets, *Mater. Chem. Front.*, 2022, **6**(17), 2422–2437, DOI: **10.1039/D2QM00091A**.

68 V. Bilovol, M. Sikora, R. Martínez García, K. Berent, M. Gajewska and A. Szkudlarek, $SrFe_{12}O_{19}/CoFe_2O_4$ Magnetic Composites: Nanoparticle Size and Effect of Annealing Temperature on Magnetic Properties, *J. Magn. Magn. Mater.*, 2022, **563**, 169987, DOI: **10.1016/j.jmmm.2022.169987**.

69 M. Petrecca, B. Muzzi, S. M. Oliveri, M. Albino, N. Yaacoub, D. Peddis, C. de Julián Fernández, C. Innocenti and C. Sangregorio, Optimizing the Magnetic Properties of Hard and Soft Materials for Producing Exchange Spring Permanent Magnets, *J. Phys. D: Appl. Phys.*, 2021, **54**(13), 134003, DOI: **10.1088/1361-6463/abd354**.

27828 | *Phys. Chem. Chem. Phys.*, 2023, **25**, 27817–27828

This journal is © the Owner Societies 2023